Brownian Motion and Large Electric Polarizabilities Facilitate Dielectrophoretic Capture of Sub-200 nm Gold Nanoparticles in Water

Clyde Midelet, Bruno Le Pioufle, Martinus Werts

Brownian motion and large electric polarizabilities facilitate dielectrophoretic capture of sub-200 nm gold nanoparticles in water

Clyde Midelet,[a,b] *Bruno Le Pioufle*[c] *and Martinus H. V. Werts**[a,b]

[a] Clyde Midelet, Dr. Martinus H.V.Werts

Univ Rennes, CNRS, SATIE - UMR 8029, F-35000 Rennes, France

[b] Clyde Midelet, Dr. Martinus H.V.Werts

École normale supérieure de Rennes, SATIE (CNRS UMR 8029), Av. R. Schuman, Campus de Ker Lann, F-35170 Bruz, France

E-mail : martinus.werts@ens-rennes.fr

[c] Prof. Bruno Le Pioufle

Ecole normale supérieure Paris-Saclay, SATIE (CNRS UMR 8029), Institut d'Alembert, F-94235 Cachan, France

Keywords: Dielectrophoresis, gold nanoparticles, microfluidics

ABSTRACT

Dielectrophoresis can move small particles using the force resulting from their polarization in a divergent electric field. In liquids, it has most often been applied to micrometric objects such as biological cells or latex microspheres. For smaller particles, the dielectrophoretic force becomes very small and the phenomenon is furthermore perturbed by Brownian motion. Whereas dielectrophoresis has been used for assembly of superstructures of nanoparticles and for the detection of proteins and nucleic acids, the mechanisms underlying DEP of such small objects require further study. This work presents measurements of the alternating-current (AC) dielectrophoretic response of gold nanoparticles of less than 200 nm diameter in water. An original dark-field digital video-microscopic method was developed and used in combination with a microfluidic device containing transparent thin-film electrodes. It was found that the dielectrophoretic force is only effective in a small zone very close to the tip of the electrodes, and that Brownian motion actually facilitates transport of particles towards this zone. Moreover, the fact that particles as small as 80 nm are still efficiently captured in our device is not only due to Brownian transport but also to an effective polarizability that is larger than what would be expected on basis of current theory for a sphere in a dielectric medium.

1. Introduction

Dielectrophoresis (DEP) is the motion of small, electrically polarizable particles in a divergent electric field. It does not require the particles to be electrically charged. It was first reported in 1951 by Pohl in his seminal paper.[1] The force driving the motion of the particles arises from their polarization in an electric field with a non-zero gradient.[2] The electric field may be an alternating electric field since the direction of the force does not depend on the sign of the electric field. Typical frequencies used are in the 10 kHz to 10 MHz range, but the limits are often of practical nature, rather than due to intrinsic physical limits.

Depending on the relative polarizabilities of the particles and their surrounding medium, the force may be directed either towards zones where the gradient of the electric field is high ("positive DEP"), or away from them ("negative DEP"). It has been shown experimentally for particles larger than 1 μm that the magnitude of the dielectrophoretic force scales with the volume of the particles,[3,4] as expected from basic DEP theory.

In recent years, microfabrication methods have enabled the generation of strong electric fields (and strong electric field gradients) in microfluidic channels via integrated micro-electrodes. This has led to the application of DEP for, *e.g.*, biological cell assembly,[5] separation of particles,[6–8] the manipulation of nanowires[9] and carbon nanotubes,[10,11] the formation of chains of gold nanoparticles,[12] the production of nanodroplets,[13] the control of a biphasic medium as a function of the dielectric properties of the phase,[14,15] the electrospinning of fibres,[16] the formation of single DNA molecule bridge,[17] and in the field of molecular electronics using 3D multilayer DNA origami structures.[18] AC dielectrophoresis appears particularly interesting for manipulating functionalised plasmonic particles in biosensing applications.[19,20] Such particles could then act as "colloidal sensors" that are mixed with a liquid sample, allowed to diffuse freely throughout the small sample volume, and finally read out optically after concentration by dielectrophoresis.[21]

As the particle diameter decreases towards nanometric dimensions, the DEP force becomes ever weaker, while the particle's motion become increasingly Brownian, *i.e.* the action of the directional DEP force is blurred away by the random forces of Brownian motion, and DEP-controlled assembly is expected to become increasingly difficult to achieve for nanoparticles. In this respect, it is at first sight somewhat unexpected that DEP-induced capturing and even assembly of nanoparticles and nanometric virus particles have been observed.[7,12]

Quantitative experimental studies of the dependence of the DEP force on particle size are rare for sub-micron particles. Most studies of DEP with submicron particles focus on the frequency-

dependence of the DEP force, which changes sign at a certain frequency of the electric field (the 'cross-over frequency').[22,23] *In situ* real-time monitoring of dielectrophoresis of sub-micron particles has been reported, mainly utilizing fluorescent polystyrene latex particles.[24–26] Positive DEP of polystyrene latex and tungsten trioxide nanoparticles has been monitored inside a microfluidic channel using confocal Raman spectroscopy, studying the E-field frequency.[27] DEP is of interest for the development of lab-on-chip analysis methods[28], and has been used to concentrate plasmonic particles for various modes of Raman spectroscopy.[27,29]

In addition to artificial sub-micron nanoparticles, DEP has recently been applied to smaller biological nano-objects: proteins,[30–34] nucleic acids,[35,36] and extracellular vesicles.[37,38] In the case of proteins and nucleic acids, the required very high electric field gradients are achieved using sub-micron and nanometer-scale electrode gaps, that concentrate the electric field gradients in extremely small volumes. One particularly suitable method for obtaining such high electric field strengths consists of applying the electric field externally and focussing it through insulating dielectric nanostructures.[30,35,39] This insulator-mediated DEP avoids direct contact of the electrodes with the biological medium. The characterization of DEP in these systems is generally in terms of the cross-over frequency of the objects, from which the DEP force at other frequencies can be estimated indirectly by applying theoretical models.[31]

In the present work, we have studied the strength and the dynamics of the DEP-controlled capture of gold nanoparticles of different diameters at the tips of thin-film microelectrodes on the substrate of a microfluidic channel. We focus purely on dielectrophoresis, in the absence of pressure-driven flow of the fluid while also avoiding electrohydrodynamic fluid motion[6,40] by choosing suitable frequencies (1…5 MHz) and amplitudes for the applied electric potential.

Gold nanoparticles were chosen as the objects of study since they are of interest for the development of *in vitro* detection schemes based on (electro)microfluidics.[41] They are readily

detected in microfluidic channels by dark-field light scattering.[42] Also, their surface may be coated with different kinds of (bio)functional molecules for analytical detection schemes.[41] In this paper, we limit ourselves to gold nanoparticles coated with lipoate (LA) ligands,[42,43] and will focus on the diameter-dependence of DEP. Lipoate-coated gold nanoparticles have been shown to be "well-behaved" colloids with respect to diffusion,[44] and colloidal stability.[45] Commercial colloidal nanoparticle dispersions are typically stabilized using citrate and other carboxylates, and the precise composition of the aqueous medium is not specified by the manufacturers. Exchange of the commercial citrate medium with an aqueous sodium lipoate solution of known composition gives access to dispersions of LA-coated nanoparticles of various diameters in aqueous phases of identical composition.

The electromicrofluidic device consists of a slab of transparent silicone elastomer with imprinted microfluidic channel on top of a fused silica substrate carrying sharply tipped[27] thin-film microelectrodes (Figure 1). Gold nanoparticles are observed utilizing "side-illuminated" dark-field contrast,[42,46,47] exploiting the high resonant light scattering cross-sections[42,45,48] of these particles. Using this configuration (Supporting Information, Figure S1) and quantitative digital videomicroscopic imaging, we were able to measure and quantify the variation of the DEP force on gold nanoparticles ranging from 80 to 150 nm. The approach that we followed is based on using the light intensity as a measure of the nanoparticles concentration. Capture of nanoparticles due to positive DEP leads to an increase of light intensity on the electrodes tips over time. When the DEP field is switched off, the previously captured nanoparticles diffuse freely, and the system returns to an equilibrium state with an evenly distributed nanoparticle concentration (Figure 1).

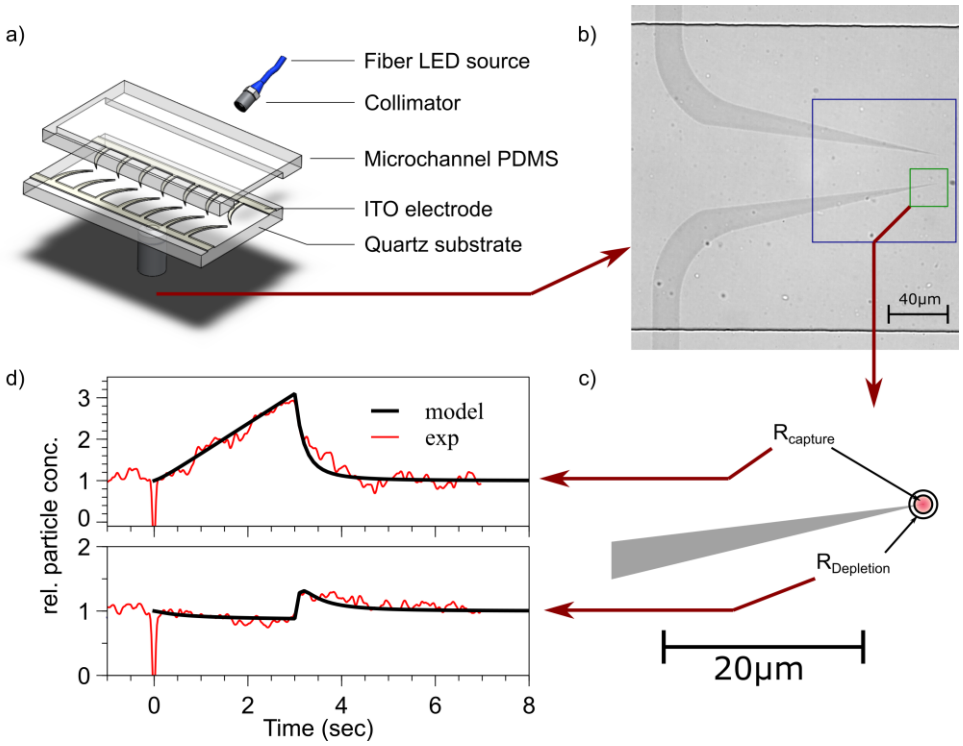

Figure 1. a) Schematic representation of the transparent microfluidic device (PDMS on quartz glass substrate with thin-film electrodes). b) Contrast-enhanced bright-field micrograph of patterned ITO microelectrodes in a PDMS microchannel filled with water. The outer blue square represents the typical 'region of interest' used for dark-field videomicroscopic recording of the electrokinetic response of nanoparticles. c) Drawing of the electrode tip. The DEP 'capture area' is represented by the red inner circle with $R_{capture}$ as radius. The outer 'depletion area' delimited by the $R_{depletion}$. d) Time-evolution of the total detected light intensities during a DEP "capture and release" cycle for the 'capture' (top) and 'depletion' (bottom) zones.

This paper is organized as follows. First, we establish the operational limits on the parameters of the applied electric potential in terms of the amplitude and frequency. These limits come on one hand from the need to conserve the integrity of the ITO electrodes (Section 2.1) and on the other from the necessity to avoid electrodynamic flows in order to observe 'pure' dielectrophoresis (Section 2.2). Next, we discuss the measurement method, and establish the reproducibility of the measurements over several microfluidic devices (Section 2.3). The method is further validated by studying the frequency dependence of DEP of latex particles, for which results are available in the literature (Section 2.4). Then we study DEP for different diameters of gold nanospheres by repeatedly capturing and releasing the particles and observing the dynamic behaviour using digital videomicroscopy (Section 2.5). Using a simple physical

model describing Brownian motion and DEP of nanoparticles in our device, we are subsequently able to understand the observed dynamic behaviour in terms of a reaction-diffusion model, from which we can estimate the relative effective electric polarizabilities of the nanoparticles.

2. Results and discussion

2.1. Robustness of the indium-tin oxide thin film electrodes

We first established the limits on the operational parameters for the applied electric potential using our microfluidic devices and aqueous gold nanoparticle dispersions. Frequencies of the AC electric potential lower than 100 kHz were rigorously avoided, because of rapid degradation of the thin layer electrodes at those frequencies.[49] Even at 500 kHz, prolonged operation at high amplitude leads to a slow degradation of the electrodes (Supporting Information, Section S3).

With newly fabricated electrodes, the capture of the particles is highly localized at the tips of the electrodes. After prolonged cycling at frequencies below 800 kHz, the region where particles are captured by DEP gradually extends from the tips along the edges of the electrode. This leads to capturing of particles all along the electrode edges instead of only at the tips (Supporting Info, Figure S2).

We found, using atomic force microscopy, that the electrodes are deteriorated by running them at low frequency, high amplitude potentials. These electrodes displayed a more pronounced roughness than newly fabricated, pristine electrodes (Supporting Information, Figures S3 and S4). The increased roughness creates additional sharply tipped “hot spots” where the electric field gradient is enhanced, and where DEP capture can take place. Whereas this roughening-enhanced DEP is useful for optimizing the yield of dielectrophoretic capture in view of potential

analytical applications, we avoid it in this study (Supporting Information, Table S1), since here we focus on precisely monitoring nanoparticle dielectrophoresis in a small and well-defined zone.

2.2. Survey of electrokinetic phenomena of nanoparticle solutions in device

It is known that the application of alternating electric fields to aqueous solutions can lead to electrokinetic phenomena other than DEP, in particular electrohydrodynamic flows, in which the entire fluid volume is put into motion via AC electro-osmosis (ACEO) and electrothermally induced flow (ETIF).[24,50,51] These electrohydrodynamic flows make direct study of dielectrophoresis more complex, and we chose to avoid them in order to be able obtain "pure" dielectrophoresis. To this end, we explored the motion of the nanoparticles in the electromicrofluidic device as a function of field frequency.

At low frequencies (< 800 kHz) and high amplitudes (> 15 V_{pp}), electro-convective motion of the colloidal solution around the electrode tips is readily observable (Supporting Information, Figure S5). This electrohydrodynamic motion is parallel to the plane of the electrodes. We found that electrically induced convective motion of the fluid is absent at frequencies above 800 kHz, for electric potential amplitudes below 15 V_{pp}. Therefore, in the remainder of this work we will exclusively utilize frequencies higher than 1 MHz and applied potential amplitudes lower than $10V_{pp}$ to rigorously avoid undesirable electrohydrodynamic effects.

2.3. Digital videomicroscopy of DEP capture-and-release cycles

In this section, we illustrate the videomicroscopic measurement of nanoparticle DEP, demonstrate the acquisition cycle and processing of the video sequences. The videomicroscopic analysis is based on the fact that the light intensity measured in each pixel in each frame is proportional to the average number of particles in the corresponding observation volume. Even though we are able to observe individual particles in the individual video frames, we do not use

particle tracking methods[52] since the particle densities in our case are too high for these methods to work reliably, especially in the "capture" zone.

Instead, we record videomicroscopic sequences while periodically switching the DEP field on and off. These video sequences are averaged into an "average" sequence, a procedure very similar to the averaging of traces in a digital oscilloscope. After injection of a solution of nanoparticles and ensuring the absence of any fluid motion, the AC electric field is applied to the electrodes for 3 seconds ("DEP ON") and then switched off for 5 seconds ("DEP OFF"). This on-off cycle is repeated for approximately 3 minutes, while recording the videomicroscopic sequence. After recording, the cycles are averaged (Figure 2). For each set of experimental parameters, three videos are recorded.

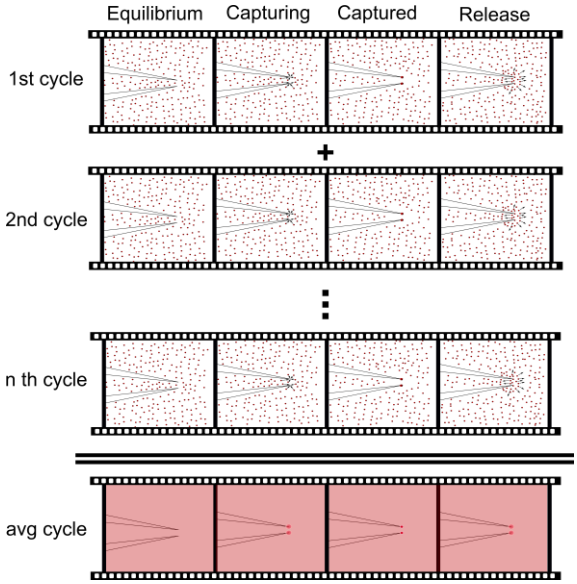

Figure 2. Schematic representation of the sequence of the experiment. A DEP "capture-and-release" cycle is repeated "n" times, while filming the microscopic images near the electrode tips. After recording the full sequence, a "cycle-averaged" video is created by adding up all frames at the same phase of the cycle, giving a videomicroscopic sequence over one DEP cycle that contains the average signal over many cycles, greatly increasing signal over noise, while averaging out the movements of individual particles.

Figure 3 contains an example of a typical measurement. Four (averaged) frames at different phases of the "DEP ON"- "DEP OFF" cycle are shown. Particles accumulate at the tips of the

electrodes (indicated using white arrows) during the "DEP ON" phase, leading to an increase in detected light intensity at the tips (Figure 3.b). Upon switching the DEP field off, the captured particles are released leading to a "flash" of nanoparticles that diffuses outward from the electrode tips (Figure 3.c).

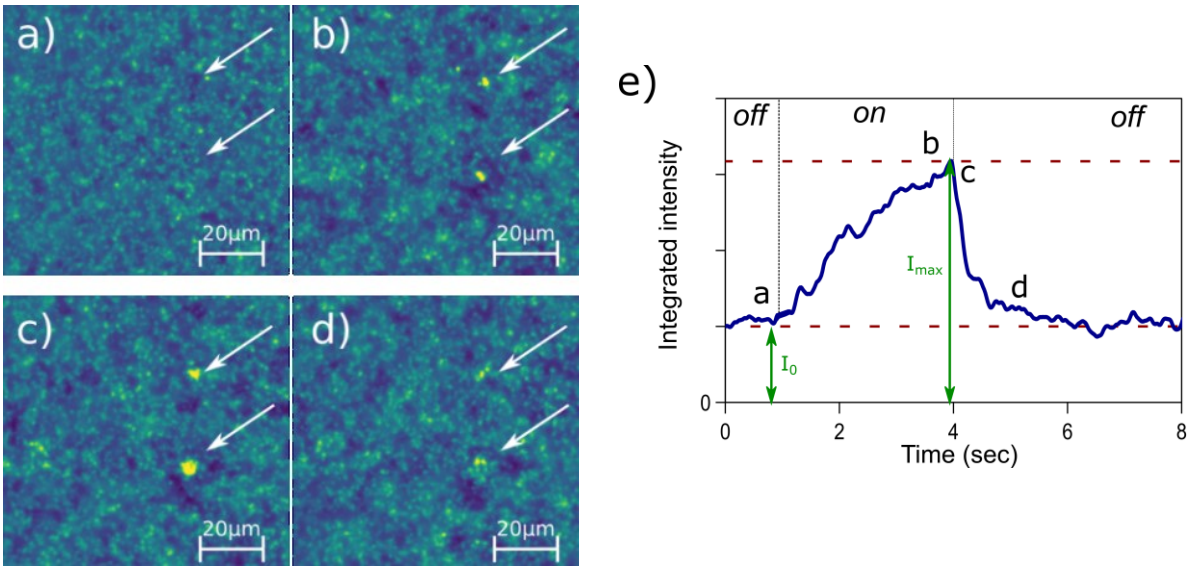

Figure 3. Real-time monitoring of dielectrophoretic capture of 100 nm gold nanospheres using dark-field videomicroscopy (50 frames-per-second), with averaging over approximately 20 'on-off' cycles. Averaged frames at different phases of the cycle: (a) at equilibrium, with E-field switched off (t = 0 s); (b) after 3 s of electric field; (c) just after t = 4 s when E-field was switched off; (d) at t = 5 s, when captured particles have partially diffused away. The zone where the intensity was monitored for capture is indicated with white arrows (circular area with a radius of 2 µm). Right panel (e): integrated intensity vs time in the monitored zone (video averaged over cycles).

We found that the region at the electrode tips where the particles are captured is well approximated by a circle with a radius of 2 µm. The integrated intensity in this zone (I) is thus a measure of the amount of particles captured. Figure 3e shows the trace of I vs time for the video sequence represented by the four frames. We define the capture ratio ϕ_{cap} as the ratio of the maximum of the integrated intensity just after release (I_{max}) to the integrated intensity at equilibrium (I_0), which is equal to ratio of the particle concentrations at capture (C_{capt}) and at equilibrium(C_0).

$$\phi_{\text{cap}} = \frac{I_{\max}}{I_0} = \frac{C_{\text{capt}}}{C_0} \qquad \text{Eq.1}$$

The capture ratio is determined precisely from the amplitude of a decay function that is fit to the decay of the intensity upon switching off the DEP field. The capture ratio ϕ_{cap} equals unity when no capture takes place (*i.e.* the equilibrium value).

To verify the repeatability of the measurement of the capture ratios between different devices, we studied a single nanoparticle dispersion, lipoate-coated gold nanoparticles of 100 nm diameter (Au100-LA) in 1 mM aqueous NaOH, at the same setting for amplitude and frequency ($6V_{pp}$, 1 MHz) over several measurement cycles and in several devices. Four devices were used. Each system was used for at least three measurements over 23 DEP "capture and release" cycles. The measurement uncertainty on the capture ratio value was estimated to be within 20% (Supporting Information, Figure S6).

2.4. Frequency-dependence of DEP capture ratio for latex spheres and gold nanoparticles

Using the methodology described above, we investigated the dependence of the capture ratio on the frequency of the electric field at constant amplitude of the applied potential. For comparison with results from literature obtained using other measurement methods, we first studied the dielectrophoresis of polystyrene particles (latex spheres). The DEP of these particles is well known to be frequency-dependent.[7,8,23,53] At constant field amplitude, the amount of captured particles decreases towards higher frequencies, since the dielectrophoretic force becomes weaker. At a certain frequency, the crossover frequency, the dielectrophoretic force changes sign, turning from positive DEP to negative DEP, meaning that DEP pushes particles away from the capture zone.

The weakening of the DEP force on latex particles with increasing frequency is indeed observed as a decrease in the capture ratio in our measurement (Supporting Information, Figure S7) While it was difficult to directly observe negative DEP (Supporting Information, Figure S8),

the crossover frequency could be sufficiently reliably extrapolated from the decreasing capture ratio with increasing frequency. The crossover frequencies, 5 MHz for 200 nm 4 MHz for 500 nm, 2 MHz for 810 nm latex spheres, were well in line with observations in literature.[4,22,23,54] Moreover, we found that the decrease of the capture ratio for the latex particles as a function of rising frequency followed the Clausius-Mossotti factor predicted by the theoretical model (Supporting Information, Section S5). This proves that our methodology yields results that are consistent with existing literature.

Applying our measurement method to gold nanoparticles, we found the capture ratio to be constant and independent of frequency in the 800 kHz - 6 MHz range (Supporting Information, Figure S9). This is in agreement with results by Honegger *et al.*[23] who determined the real part of the Clausius-Mossotti factor of gold nanoparticles of 100, 150, 200 and 250 nm diameter, and found it to be independent of frequency, with a constant value near 1. The Clausius-Mossotti factor for gold nanoparticles is expected to be unity for frequencies well beyond 1 GHz, as a result of their conductive core.[55] On basis of this finding, we decided to keep the working frequency fixed at 1 MHz.

2.5. Dielectrophoretic capture of Brownian gold nanoparticles in water: dependence of the DEP capture ratio on the AC electric field amplitude and the nanoparticle diameter

We now discuss the results of the quantitative measurement of the DEP capture ratios for 80 nm, 100 nm and 150 nm diameter gold nanospheres as a function of the amplitude of the AC electric potential applied to the electrodes. These measurements were carried out using a fixed frequency of 1 MHz. Experimental settings were kept constant for all particle diameters and amplitudes: temperature (298 K), solution conductivity (1×10^{-2} S m^{-1}), electric field switching sequence (3 s "ON", 5 s "OFF"), camera frame rate (50 fps), device geometry (electrode separation 20 µm, channel height 20 µm). As described above, videomicroscopic sequences

were recorded for each data point, processed, and the corresponding capture ratio was determined.

The resulting set of experimental capture ratios as function of nanoparticle diameter and electric field amplitude is shown in Figure 4. The capture ratios rise quadratically with the amplitude of the applied AC potential. We chose to stay at sufficiently low amplitudes to ensure this quadratic behavior, as well as avoiding unnecessary deterioration of the ITO electrodes.

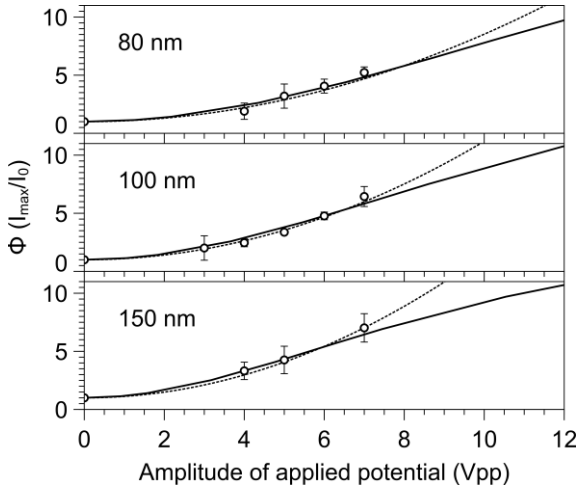

Figure 4. Experimental DEP capture ratios (black circles) for gold nanoparticles in aqueous solution as a function of the amplitude of the AC potential applied to the electrodes, quadratic fits to the experimental data (dotted lines) and capture ratios from numerical modelling (solid lines). Each experimental point corresponds to at least three measurements in different devices (f = 1 MHz). Fit between model and experiment is obtained via adjustment of a single parameter, *i.e* κK_{pol} (see Text). All other model parameters were kept fixed to their pre-determined values (capture radius: 2 µm; nanoparticle diffusion coefficients from the Stokes-Einstein-Sutherland relation; DEP ON: 3s, DEP OFF: 5s).

The main experimental observations on the dielectrophoresis of sub-200 nm gold nanoparticles in our microfluidic architecture can be summarized as follows:

- The dielectrophoretic capture is concentrated in a small area at the tip of the electrodes
- The dielectrophoresis is independent of frequency over the frequency range studied.

- At low field amplitudes the capture ratio depends quadratically on the electric field amplitude.

We developed a simple physical model of the dielectrophoretic capture of Brownian, sub-200 nm gold nanoparticles that reproduces the experimental observations.

The time-averaged DEP force experienced by a polarizable particle of arbitrary size, shape and composition in a medium of different polarizability in a divergent AC electric field is well known.[56]

$$\langle \mathbf{F}_{\mathrm{DEP}} \rangle = \frac{1}{4} v \mathrm{Re}[\tilde{\alpha}] \nabla |\mathbf{E}|^2 \qquad \text{Eq. 2}$$

In this expression, v is the volume of the particle; $\tilde{\alpha}$ is the effective complex polarizability of the particle in the medium, of which the real part translates into the DEP force.

In the context of our measurement, we control the frequency (radial frequency, ω) and amplitude (U_0) of the electric potential applied to the electrodes,[1] and measure the effect of dielectrophoresis on different particle systems, while keeping the same geometry of the device. The electric field can be written $\mathbf{E} = U\mathbf{G}$, such that $\mathbf{G}$ contains the information on the topology of the field, and U is the experimentally applied amplitude. We further introduce $K_{pol} = v\mathrm{Re}[\tilde{\alpha}]$. This product of the particle volume v and its effective polarizability could be loosely referred to as the "dielectrophoretic susceptibility" of the particle. Thus, equation 2 can be written as follows.

$$\langle \mathbf{F}_{\mathrm{DEP}} \rangle = \frac{1}{4} K_{\mathrm{pol}} U^2 \nabla |\mathbf{G}|^2 \qquad \text{Eq. 3}$$

The sub-200 nm particles that are studied in this work undergo significant Brownian motion. The steady, directional DEP force is thus perturbed by the random Brownian force on the individual particles. At the microscopic scale, the overall behaviour of Brownian particles in a

[1] We express as 'peak-to-peak' voltages, *i.e.* $2V_{pp}$ corresponds to an amplitude of 1 V

DEP field has been described with the Fokker-Planck (or Smoluchowski) equation.[24,50] The Smoluchowski equation can be rewritten into a diffusion-advection equation.[57] Such a diffusion-advection description has been applied in simulations of DEP in combination pressure-driven and electrohydrodynamic flows.[58,59] We apply one further approximation (tentatively called the "chemist's approximation"): we replace the DEP-force related advective term by a spatially-dependent capture rate. This approximation can be made since the DEP force is strongly localized very near the tip of the electrode and always pointing towards the tip of the electrode (Supporting Information, section S7).

Far away from the electrode, the force is negligible and pure diffusion dominates. The diffusion of the nanoparticle concentration distribution is characterized by the Fickian diffusion coefficient D ($m^2\ s^{-1}$), given by the Stokes-Einstein-Sutherland relation.[60–62] In the absence of a DEP force field, all particles diffuse freely and the concentration distribution of these 'free' particles, $c = c(x, y, z, t)$, thus follows the simple diffusion equation,

$$\frac{\partial c}{\partial t} = D\nabla^2 c \qquad \text{Eq. 4}$$

A particle that comes under the influence of the DEP force and does not escape as a result of Brownian motion will end up on the tip of the electrode. The probability that the capture eventually happens is proportional to the magnitude of the DEP force. On the ensemble level (the average of the contributions of individual particles) this probability can be represented with a capture rate, which we call k_{cap}. Within the DEP "capture zone", the evolution of free particles is described by a diffusion-reaction equation:

$$\frac{\partial c}{\partial t} = D\nabla^2 c - k_{\mathrm{cap}} c \qquad \text{Eq. 5}$$

The spatially-dependent capture rate is assumed to be proportional to the (effective) magnitude of the dielectrophoretic force, which enables us to write:

$$k_{\text{cap}} = \kappa K_{\text{pol}} U^2 \qquad \text{Eq. 6}$$

K_{pol} is the term describing the polarizability of the particle in its medium. κ is a proportionality factor that links k_{cap} to the topology of the DEP force field. It translates the probability of a particle at a certain position in the DEP force field ending up captured when continuing its motion under the influence of the DEP force and the random Brownian force. This factor, κ, is constant throughout this work, since we use always devices with the same electrode configuration. This enables relative measurements of K_{pol}.

For a spherical particle of radius r having a complex permittivity $\tilde{\varepsilon}_p$ in a medium $\tilde{\varepsilon}_m$ (assuming an infinitely thin frontier between particle and medium), the following equation has been derived.

$$K_{\text{pol}} = 4\pi\varepsilon_m r^3 \text{Re}\left[\tilde{f}_{\text{CM}}\right] \text{ with } \tilde{f}_{\text{CM}} = \frac{(\tilde{\varepsilon}_p - \tilde{\varepsilon}_m)}{(\tilde{\varepsilon}_p + 2\tilde{\varepsilon}_m)} \qquad \text{Eq. 7}$$

This equation features the Clausius-Mossotti factor $\tilde{f}_{\text{CM}}$ that was mentioned above, and whose behaviour for polystyrene and gold nanoparticles is discussed in more detail in the Supporting Information (Section S5).

The topology of the field gradient is furthermore represented in an approximate manner by the spatial distribution of k_{cap}. In our model, this probability is taken to be zero outside of the zone where the DEP force is significant and to have a constant value inside. This means that when a particle enters this "DEP zone", there is a certain probability that it is captured (but it also has a probability to escape the zone thanks to Brownian motion).

The “DEP zone” is modelled to be a constant value within a hemisphere of radius R_{cap} centred around the electrode tip. (Figure 5). When the DEP field is switched off, k_{cap} is set to zero everywhere, and all capture particles are assumed to be concentrated in a thin disk. Finite-element calculations of the electric field in our device architecture (Supporting Information,

section S7) showed that the DEP force only has significant magnitude very close to the electrodes. The DEP force is always directed towards the tip of the electrode. This is in agreement with the observation that DEP capture only takes place in a small circular area near the tips of the electrodes.

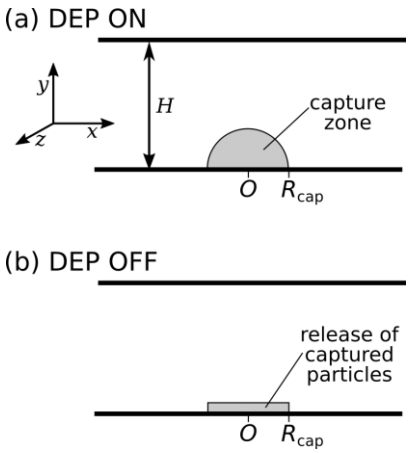

Figure 5. Schematic of the geometry of the system used in numerical modelling (cross-section in the *xy* plane at $z = 0$). (a) Hemisphere where the particles have a non-zero probability of being captured during the "DEP ON" phase. (b) Initial condition for the free diffusion upon entering the "DEP OFF" phase

Our reaction-diffusion model of dielectrophoresis of Brownian particles was solved numerically for the geometry and boundary conditions corresponding to our electro-microfluidic device. The solution describes the ensemble behaviour in terms of the spatial and temporal distribution of the particle concentration (number density), *i.e.* the collective average result of the motions of individual particles.

In Figure 6 the evolution of the radial nanoparticle concentration profile around the tip of the electrode is shown for a 2 μm thin layer above the substrate, for a given k_{cap} and D. During the "DEP capture" phase, particle density builds up in the area at the tip of the electrode. Simultaneously, there is some depletion of nanoparticles just outside this capture area, due to mass transfer limitation, *i.e.* diffusion of particles is too slow to replenish the particles that have been dielectrophoretically captured at the electrode tips.

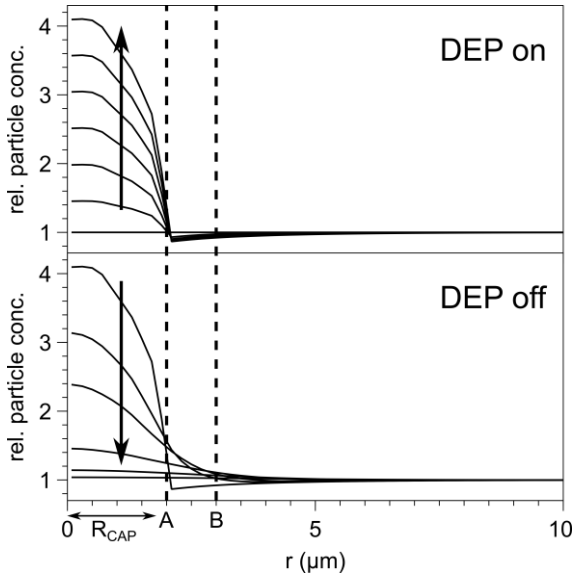

Figure 6. Example of a numerical result of the time-evolution of the relative nanoparticle concentration near the tip of the electrode: radial concentration profiles relative to the center of the capture zone. The labels "A" and "B" indicate the limits of the inner capture zone and the outer "depletion disk", respectively (corresponding to $R_{capture}$ and $R_{depletion}$ in Figure 1). Top: capture of particles by positive dielectrophoresis. Bottom: free diffusion of particles after release of the DEP field. Model parameters: 100 nm nanoparticles, water at 298K, capture radius 2 µm, capture rate 0.8 s^{-1}.

When integrating the particle concentration in the inner capture area, and the particle concentration in the ring just around this area, we obtain the evolution of the integrated intensity of these two areas over time, which can directly be compared with experiment. As can be seen in Figure 7, there is close agreement between experimentally obtained DEP capture curves and model curves. Also, the depletion next to the capture zone is reproduced.

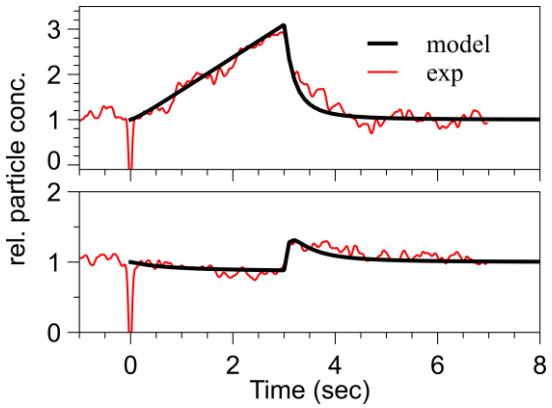

Figure 7. Time evolution of the particle concentration. Comparison of model (black) and experiment (red). Capture of 100 nm gold nanoparticles in water at 298K on the tip of electrode (top) and depletion in a ring just outside the capture zone (bottom). Experiment: amplitude 5 V_{pp}, theory: capture rate 0.8 s^{-1}.

A series of numerical simulations was carried out using our model, varying k_{cap} for each nanoparticle diameter. As simulation parameters, we used the 3 s "DEP ON"/5 s "DEP OFF" cycle from the experiment. For each of the three particle diameters, the corresponding diffusion coefficient was set, and then the capture ratios were evaluated for different values of k_{cap}. This yields the evolution of the capture ratio as a function of k_{cap}, for each nanoparticle diameter studied.

For direct comparison with experiments, k_{cap} is converted to an applied electric potential amplitude using Equation 6, so that we can plot the capture ratio as a function of applied potential amplitude. The conversion is done by choosing a value for the factor κK_{pol} that gives the best fit between experiment and model for a given nanoparticle diameter (Figure 4). For each nanoparticle diameter studied, a different value for κK_{pol} is obtained. There is agreement between the experimentally measured capture ratios and those obtained from our model (Figure 4).

The numerically modelled capture ratios have a quadratic behavior as a function of electric potential amplitude at low amplitudes, and level off at higher amplitudes as a result of nanoparticle depletion due to mass transport limitation. This depletion effect is more pronounced for larger particles. The experimental observations were done at sufficiently low amplitudes to still be in the non-depleted quadratic regime, where the Brownian motion is still sufficiently potent to supply new particles to be captured, enabling accumulation of measurable amounts of particles.

In order to fit the numerically modelled capture ratios to the experimental data, the $k_{\mathrm{cap}}$of the model is related to the amplitude of the applied potential *U*. This determines κK_{pol}. The coefficient κ only depends on the electric field topology and is independent of the nanoparticles.

We may thus determine relative values of K_{pol} for nanoparticles, by dividing the κK_{pol} by a reference value. Here, we take the 100 nm particles as the reference value. Figure 8 displays the evolution of K_{pol}, a measure of the susceptibility of the nanoparticles to dielectrophoresis, as a function of gold nanoparticle diameter.

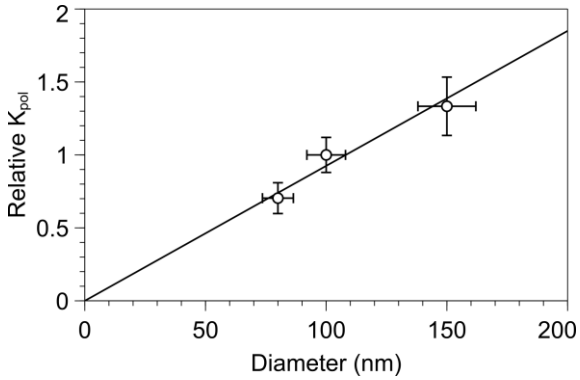

Figure 8. Relative dielectrophoretic susceptibility K_{pol} as a function of gold nanoparticle diameter (circles). The K_{pol} values are relative to the value of 100 nm particles. The solid line suggests a linear relation between K_{pol} and nanoparticle diameter.

For sufficiently large spheres, K_{pol} is expected to depend on the volume (see Equation 7), *i.e.* vary as diameter cubed. This is clearly not the case here; the dependence seems to be linear. We speculate that in the size range 200 nm to 1 μm the dependence of K_{pol} on diameter evolves gradually from linear to cubic. The break-down of the cubic dependence for sub-200 nm particles may be explained that in the derivation of Equation 7 for spherical particles, the electric double layer around the particles is approximated as a surface conductivity at the infinitely thin particle-medium interface. This is justified for sufficiently large particles (> 1 μm), where the electric double layer ion cloud is thin compared to the particle diameter, but is expected to break down for smaller particles.[63]

The linear dependence of K_{pol} on diameter means that K_{pol} falls off less radically for submicron nanoparticles than expected on basis of the usual model of the dielectrophoretic force for spheres. There are therefore two reasons why very small objects (nanoparticles, proteins, polymers) can still be captured in dielectrophoretic processes: Brownian motion bringing the

objects close to the zone of effective capture and breakdown of the cubic dependence of the dielectrophoretic force for small particles.

3. Conclusion

Through *in situ*, real-time observations on well-defined gold colloids using dark-field videomicroscopy in combination with physicochemical modelling, we explain why small gold nanospheres (in the present case: as small as 80 nm diameter) can still be effectively captured and assembled by dielectrophoresis in a microfluidic system. If one were to extrapolate the often-cited cubic dependence of the dielectrophoretic force on sphere radius from micrometre to sub-200 nm nanoparticles, the DEP force would be predicted to be exceedingly weak.

However, near the tips of microelectrodes, very high electric field gradients exist and Brownian motion is efficient in transporting smaller particles towards these zones where the particles are captured by DEP. The capture zones are limited to the regions very near (< 5 μm) the electrodes; the DEP force is negligible outside these zones. The DEP force on the gold nanoparticles was found not to depend on the frequency of the electric field in the 800 kHz – 5 MHz band studied. Interestingly, we found that the DEP force for these sub-200 nm particles does not display a cubic dependence on particle diameter, but a linear dependence. This is likely a manifestation of the increasing influence of the electric double-layer ion cloud around the particles[56,63,64] as the particle diameter decreases. The resulting higher electric polarizability might be further enhanced by the high conductivity of the gold core.

This interpretation suggests that changing the extent of the double layer by changing the ionic strength may yield further insight into the mechanism of DEP for nanoparticles. The methodology of the present paper paves the way for such studies. Interpretation of the experimental capture-release data in terms of the capture-diffusion model provides access to

the capture rate constant, which is proportional to the dielectrophoretic susceptibility K_{pol}. In the present work, we treat K_{pol} purely as an empirical parameter, without any preconceived theoretical model. The next step is to perform measurements of gold nanoparticles in aqueous media of varying ionic strength and composition to make the connection to newly developed theoretical models.[65,66] The contribution of surface conductance to the overall polarizability may be expected to be negligible for conducting particles, further highlighting the expected importance of the diffuse part of the electric double layer in the DEP of nanoparticles. An interesting question is the interplay between the polarization of the highly conductive gold core and the polarization of the electric double layer. Also, the effect of different types of surface functionalization of the gold nanoparticles needs investigation, as these will impact surface conductance and the structure of the electric double layer.

In addition to utilizing the methodology to further study gold nanoparticles, we are presently investigating ways to improve the signal-to-noise ratio of the nanoparticle detection. The dark-field scattering contrast used in the present work is limited to gold nanoparticles larger than approximately 80 nm, although the use of a more intense illumination source may give access to slightly smaller particles. Transmitted light extinction contrast may be used for imaging the spatial concentration distribution of gold nanoparticles as small as 13 nm.[44] A better understanding of the dielectrophoresis of sub-200 nm Brownian nanoparticles in aqueous media will aid in the further development of DEP-based methods for nanoparticle characterization[67–69], separation[8] and assembly of superstructures.[9,12,70]

4. Experimental section

4.1. Aqueous dispersions of nanoparticles

Aqueous colloidal dispersions of gold nanospheres of 80, 100 and 150 nm diameter, stabilized by carboxylic acids, mainly citric acid, were obtained from a commercial source

(BBInternational, Cardiff, Wales, UK). These particles are referred to as Au80, Au100 and Au150, respectively. An aqueous solution of 0.2 mM sodium lipoate (NaLA) and 1 mM NaOH was prepared using racemic (±)-α-lipoic acid (LA, Sigma, 0.2 mM) and NaOH (1.2 mM) in pure water. The conductivity of this solution was determined to be 1 x 10^{-2} S m^{-1}.

The colloidal gold particles were coated with lipoate by mixing them with the aqueous NaLA-NaOH solution. Samples were centrifuged (Mikro 220R, Hettich) for 30 min at 603 x *g* for Au80, 514 x *g* for Au100 and 450 x *g* for Au150. Then the supernatant was removed and replaced (90% of the volume) by the aqueous NaLA-NaOH solution. This centrifugation-redispersion was repeated three times, and dispersions of lipoate-coated gold nanoparticles were obtained: Au80-LA, Au100-LA and Au150-LA. The concentrations of nanoparticles in the stock solutions and also in DEP experiments were 8.74 x 10^9 particles mL^{-1} for Au80, 4.13 x 10^9 particles mL^{-1} for Au100 and 1.38 x 10^9 particles mL^{-1} for Au150. The nanoparticle samples were characterized using optical microscopy (Supporting Information, Section S10), confirming their integrity.

Aqueous colloidal suspensions of fluorescent latex spheres of 200 nm (yellow-green fluorescence) and 500 nm ("polychromatic" red fluorescence) diameter were obtained from a commercial source (Polysciences). Rhodamine-dyed latex particles,[71] 810 nm, were a gift from R. Antoine (ILM Lyon). The latex particles are referred to as PS200, PS500 and PS810, respectively. The concentration of latex spheres in the stock solution were 5.68 x 10^{12} particles mL^{-1} for PS200 and 3.64 x 10^{11} particles mL^{-1} for PS500. In the DEP experiments, latex spheres were to have concentration of particles similar to Au100-LA. The dilution was achieved, as before, using 0.2 mM lipoate in 1 mM NaOH in pure water to work with the same physicochemical environment.

4.2. Electromicrofluidic device fabrication

Electromicrofluidic devices were built from two parts: a quartz substrate with lithographically patterned transparent thin-film electrodes (indium tin oxide, ITO) and a microfluidic chamber to contain the colloidal solutions. The small gap between two tips of electrodes (20 μm) permits application of high electric field gradient in a very localised area.

Electrodes were patterned on indium-tin oxide-coated quartz slides (170μm thick, ACM, Viliers St. Frédéric, France) having a 100 nm layer of ITO. Slides were rinsed with acetone, isopropanol and Milli-Q water, and dried. Positive photoresist "S1805" (Rohm and Haas, USA) was deposited onto the substrate by spin coating for 30 s at 1000 rpm with 100 rpm s^{-1} acceleration. The resist layer was subsequently dried on a hot plate, 115°C for 60 s. The thickness of photoresist obtained is near 1100 nm. The photoresist was exposed to UV light (i-line-365nm; 180 mJ cm^2 dose) on an MJB4 mask aligner (Süss MicroTech, Germany) using a chrome quartz mask (JD Photo-data, UK) of the electrode design. The exposed resin was removed from the ITO substrate (70 s, in pure developer "MF319" from Rohm and Haas). Wet etching of the ITO layer was achieved using 37% v/v HCl (aq) (200mL + 50mL of water), at 40°C for 4 min 30 s for 100 nm ITO (etching rate of 0.37 nm s^{-1}). The last step is very sensitive to the concentration of HCl, temperature and also the etching time. Correct etching of the ITO was routinely confirmed by measuring the conductivity at the surface.

A final solvent cleaning (acetone, isopropanol, water, drying) was done in order to remove the photoresist and to obtain a clean substrate with ITO electrodes. After this last step, the thickness of the ITO layer was determined with a profilometer. Before each use, the ITO electrode substrates were cleaned using a low-pressure air plasma for 5 minutes (Harrick Plasma Cleaner/Sterilizer PDC-002, USA). They were then treated with diluted gold etch solution (151 mM potassium iodide, 25 mM I_2 in water) for 4 min at temperature room (19°C), to remove

any remnant gold nanoparticle deposits. Finally, they are thoroughly rinsed with deionized water and dried under a filtered, compressed air stream.

Microfluidic circuits were moulded into an optically transparent silicone elastomer. For fabrication of the mold, a 20 μm thick SU-8 layer (Microchem SU-8 3025) was spin-coated on top of a 2" silicon wafer and patterned using photolithography as stated previously (i-line-365nm; 180 mJ cm^2 dose). Polydimethylsiloxane (PDMS Sylgard 184 - Dow Corning) was chosen as the material for the microfluidic chip. A 10:1 mix of PDMS and its curing agent is degassed under reduced pressure (2 hours) and then poured on top of SU-8 molds in a Petri dish. The Petri dish containing the mold and the PDMS is once again degassed and cured for one hour at 70°C before the PDMS is peeled off the mold. Finally, holes for the inlets/outlets of the microfluidic chips are punched in the PDMS slab.

The electromicrofluidic device was assembled by positioning the PDMS microfluidic circuit on top of the ITO/quartz electrode substrate. Prior to assembly, the bottom of the PDMS circuit was wetted with a small quantity of ethanol which enables free movement of the PDMS on top of the substrate. Positioning was then achieved manually, monitoring alignment of the microfluidic channel and the electrode structure using an optical microscope. Once aligned, the device was left to dry, and microfluidic tubing was connected. The microfluidic circuit was operated using pressure driven flow. Fine control of the pressure at the exit of the microfluidic circuit (and hence the pressure difference between entrance and exit) was achieved using a screw syringe (total volume 60 mL, Jeulin, Evreux, France) filled with air. Air pressure was monitored using a digital pressure meter (Jeulin).

4.3. Optical microscopic set-up

The microfluidic volume inside the device was observed through an Olympus IX71 inverted microscope using a moderate magnification objective (20x, N.A. = 0.4). Transmitted light illumination was used for conventional brightfield imaging of the electrodes and the overall

device structure. Gold nanoparticles in liquid dispersion were observed via their resonant light scattering using the previously developed side-illuminated dark-field contrast.[42,46,72] Latex particles were observed using standard epifluorescence contrast.

For dark-field illumination, the collimated light of a fiber-coupled high-power white LED (Thorlabs) is focused into the PDMS slab from the side. The slab acts as a light guide as a result of total internal reflection (Supporting Information, Figure S1) leading to clean dark-field illumination. The angle of incidence was optimised to reduce stray light to have the best dark field with minimal background signal. The white LED for dark-field observation gives a broad spectral coverage, compatible with the plasmon resonances of the particles. The 150 nm and 100 nm gold nanoparticles display a very broad plasmon resonance in their extinction and scattering spectra (Supporting Information, Figure S12), which is red-shifted with respect to the plasmon resonance observed with smaller nanospheres. Scattered light is observed through the quartz glass/ITO electrode substrate using a microscope objective.

For microscopy using epifluorescence contrast, a conventional wide-field configuration was used with an LED (470nm) from Thorlabs (New Jersey, United States) as the excitation light source. A filter cube (Olympus U-MWB2) separates illumination at 470 nm and fluorescence emission at wavelengths longer than 500 nm.

4.4. Optical videomicroscopy

Microscopy image sequences (videos) were acquired using a Ximea CMOS monochrome camera (xiQ-USB3, MQ042RG-CM) having a CMOSIS CMV4000 image sensor (2048x2048 pixels, 15.9 mm diagonal). LED illumination and electric field switching were controlled using home-built real-time trigger electronics based on an Arduino Uno board running custom software. The timing sequence was set over USB using a Python script running on a personal computing (PC) workstation. Electric field was generated by applying the output of a function generator (Centrad GF266, ELC, France) to a selected pair of ITO electrodes on the substrate.

The function generator generates a sine wave of specified frequency and amplitude whose values are set via the PC workstation. The electronics allow for a fully synchronized video acquisition cycle, during which the electric field is switched on and off at precisely defined time points.

Typically, image frames of 512x512 pixels are recorded (corresponding to a 137 µm x 137 µm area in the object plane). Videos were acquired at 50 frames per second, switching the electric field on and off over cycles with a period of 8 s (5 s 'OFF', 3 s 'ON'). Three separate videos of approximately 3 minutes were recorded for each experiment. Precise synchronization of the electric field switching with video acquisition was verified by briefly blinking the LED illumination (10 ms) which enables detection of the beginning of the DEP cycle ($t_0 = 0$ s). The timing of the blinking (and the electric field switching) was found to be precise to a single frame (better than 20 ms).

The recorded videomicroscopy sequences were processed using home-written software running on Python 3.5.2 (Anaconda 4.1.1, 64-bit, Continuum Analytics, USA), with the 'numpy', 'scipy' and 'matplotlib' libraries,[73,74] and ‘tifffile.py’ for reading TIFF format video files into computer memory.[75]

The dark current in all camera pixels was measured by recording an image sequence with the dark-field illumination switched off. All recorded video frames were first corrected by subtracting this electric dark current in each pixel. With the illumination switched on, a constant background image, consisting of residual scattering of the device structure (electrodes, microfluidic channel walls, debris) was observed. The average image of this immobile background was subtracted, leaving only the foreground image (corresponding to the mobile nanoparticles) for the analysis. As a result of the homogeneity of the dark-field illumination (refocussed output of a fiber-coupled LED) and the homogeneity of the imaging system over

the observation area (center 512x512 pixel region of microscopic image), vignetting was absent, and no shading correction was required.

4.5. Numerical modelling

The time-evolution of the spatial distribution of nanoparticles near the DEP electrode tip is modelled numerically using a simple diffusion-reaction system, as explained above. The local concentration of free nanoparticles is designated $u = u(x, y, z, t)$ and $v = v(x, y, z, t)$ represents the local concentration of particles that have been captured by DEP. The free nanoparticles diffuse with a constant isotropic Fickian diffusion coefficient D. The process of nanoparticles being trapped onto the small area at the tip of the electrodes is represented as a reaction transforming free particles into captured ones, characterized by rate constant $= k(x, y, z, t)$.

$$\begin{cases} \frac{\partial u}{\partial t} &= D\nabla^2 u - ku \\ \frac{\partial v}{\partial t} &= +ku \end{cases} \qquad \text{Eq. 8}$$

The system is considered to be infinite in the x and z directions, and of limited height H in the y direction (refer to Figure 5 for a diagram of the simulation geometry). In the numerical method, this is approximated by choosing a domain of width L sufficiently large for x and z and applying Dirichlet boundary conditions (*i.e.,* the values at these boundaries are kept constant at a particular value, providing a constant-concentration reservoir in the x and z directions). Numerical tests demonstrated L = 12 μm to be a reliable choice for our system.

$$\begin{aligned} &x, z \in [-L/2\,, L/2] \\ &u = c_{eq}, \text{ at } x = -L/2\,, x = L/2\,, z = -L/2\,, z = L/2 \end{aligned} \qquad \text{Eq. 9}$$

In the y direction, the particle flux is set to zero at the bottom and top of the microchannel (Neumann 'zero-flux' boundary condition). In our case, we have channel height $H = 20\ \mu m$.

$$y \in [0, H]$$
$$\frac{\partial u}{\partial y} = 0, \quad \text{at } y = 0, y = H \qquad \text{Eq. 10}$$

In our model, we start with an initial condition at $t = 0$ where the system is at equilibrium, *i.e.* the concentration of free particles is the same throughout the sample, and no particles have been captured. The value of C_{eq} is arbitary, since our experiment gives the relative concentration, and a convenient choice is $C_{\text{eq}} = 1$.

$$u(x, y, z, t = 0) = C_{\text{eq}}$$
$$v(x, y, z, t = 0) = 0 \qquad \text{Eq. 11}$$

The variable v keeps track of how many particles have been captured during the phase where the DEP field is active. The process of a particle coming under the influence of the DEP force and ultimately being captured at the electrode (in spite of its Brownian motion) is modelled using the approximation that k has a constant value within a radius R_{cap} around the tip of the electrode and is zero everywhere else. This reflects the notion that the DEP force is only significant very close to the electrode tip and does not influence the motion of the particles farther away. Switching the DEP field on and off is reflected by the temporal dependence of k. The DEP field is on between $t = 0$ and $t = t_{\text{off}}$, and is subsequently switched off.

$$\begin{cases} k = 0, & t > t_{\text{off}} \\ k = 0, & t \in [0, t_{\text{off}}] \wedge x^2 + y^2 + z^2 > R_{\text{cap}}^2 \\ k = k_{\text{cap},} & t \in [0, t_{\text{off}}] \wedge x^2 + y^2 + z^2 \leq R_{\text{cap}}^2 \end{cases} \qquad \text{Eq. 12}$$

Simultaneously, at $t = t_{\text{off}}$ all captured particles are released as a thin flat disk with radius R_{cap} and a minimal height h, which we chose to be the height of a single elemental volume in our solver. We numerically achieved this transfer from "captured" to "free" particles by summing all xz planes of v over all y and adding this sum plane to the bottom plane of u. Subsequently all elements of v are set to 0. In essence, we sequentially solve two partial differential equation systems, the first representing the DEP capture phase in a diffusion-reaction system, the second

a pure diffusion equation of the released particles, using the results of the first PDE as the initial condition.

This system of partial differential equations was solved numerically in a regular cubic mesh in Cartesian coordinates using the finite-volume method implemented by the FiPy library[76] (version 3.1.3.dev531+gd4b7593, Anaconda 4.4.10, Python 2.7.15-condaforge, 64-bit Linux). The choice of the Cartesian coordinates and the regular mesh was guided by (i) limitations in the code concerning the use of cylindrical coordinates, and (ii) facilitation of post-processing of the solution on a regular mesh, in spite of the higher computational cost. The computational cost was somewhat alleviated by using symmetry and calculating only one quadrant of the solution.

Supporting Information

Supporting Information is available from the Wiley Online Library or from the author.

Acknowledgements

This work was supported through a Ph.D. fellowship funded jointly by ENS Rennes and *Région Bretagne* (ARED programme). Additional funding from the Institut d'Alembert (Cachan, France, project "CAFEMICRO") is gratefully acknowledged. We thank R. Antoine (Institut Lumière et Matière, CNRS and University of Lyon) for sending us a sample of Rhodamine-dyed polystyrene latex, and T. Gwénolé and J. P. Guin (LARMAUR laboratory, University of Rennes) for AFM measurements of our thin-film electrodes.

Conflict of Interest

The authors declare that there is no conflict of interest.

References

[1] H. A. Pohl, *J. Appl. Phys.* **1951**, *22*, 869.
[2] T. B. Jones, *IEEE Eng. Med. Biol. Mag.* **2003**, *22*, 33.
[3] J. Voldman, R. A. Braff, M. Toner, M. L. Gray, M. A. Schmidt, *Biophys. J.* **2001**, *80*, 531.
[4] M. T. Wei, J. Junio, D. H. Ou-Yang, *Biomicrofluidics* **2009**, *3*, 012003.
[5] J. Cottet, A. Kehren, S. Lasli, H. Lintel, F. Buret, M. Frénéa-Robin, P. Renaud, *Electrophoresis* **2019**, *40*, 1498.
[6] A. Ramos, H. Morgan, N. G. Green, A. Castellanos, *J. Phys. D: Appl. Phys.* **1998**, *31*, 2338.
[7] H. Morgan, M. P. Hughes, N. G. Green, *Biophys. J.* **1999**, *77*, 516.
[8] P. R. C. Gascoyne, J. Vykoukal, *Electrophoresis* **2002**, *23*, 1973.
[9] K. D. Hermanson, S. O. Lumsdon, J. P. Williams, E. W. Kaler, O. D. Velev, *Science* **2001**, *294*, 1082.
[10] S. Banerjee, B. E. White, L. Huang, B. J. Rego, S. O'Brien, I. P. Herman, *J Vac Sci Technol B* **2006**, *24*, 3173.
[11] J. Sun, Z. Guo, C. Wang, N. Gu, *ChemPhysChem* **2005**, *6*, 2485.
[12] C. Leiterer, S. Berg, A. P. Eskelinen, A. Csaki, M. Urban, P. Törmä, W. Fritzsche, *Sens. Actuators B Chem.* **2013**, *176*, 368.
[13] T. B. Jones, M. Gunji, M. Washizu, M. J. Feldman, *J. Appl. Phys.* **2001**, *89*, 1441.
[14] J. Lee, B. Lee, S. Song, J. Song, *Part. Part. Syst. Charact.* **2019**, *36*, 1800470.
[15] S.-H. Hong, T.-Z. Shen, B. Lee, J.-K. Song, *Part. Part. Syst. Charact.* **2017**, *34*, 1600344.
[16] D. Lukas, A. Sarkar, P. Pokorny, *J. Appl. Phys.* **2008**, *103*, 084309.
[17] M. Kumemura, D. Collard, C. Yamahata, N. Sakaki, G. Hashiguchi, H. Fujita, *ChemPhysChem* **2007**, *8*, 1875.
[18] B. Shen, V. Linko, H. Dietz, J. J. Toppari, *Electrophoresis* **2015**, *36*, 255.
[19] M. Loumaigne, R. Praho, D. Nutarelli, M. H. V. Werts, A. Débarre, *Phys. Chem. Chem. Phys.* **2010**, *12*, 11004.
[20] N. Nerambourg, R. Praho, M. H. V. Werts, D. Thomas, M. B. Desce, *Int. J. Nanotechnol.* **2008**, *5*, 722.
[21] M. H. V. Werts, F. Allix, O. Français, C. Frochot, L. Griscom, B. Le Pioufle, M. Loumaigne, J. Midelet, *IEEE J. Sel. Top. Quantum Electron.* **2014**, *20*, 102.
[22] N. G. Green, H. Morgan, *J. Phys. Chem. B* **1999**, *103*, 41.
[23] T. Honegger, K. Berton, E. Picard, D. Peyrade, *Appl. Phys. Lett.* **2011**, *98*, 181906.
[24] D. J. Bakewell, H. Morgan, *Meas. Sci. Technol.* **2004**, *15*, 254.
[25] D. J. Bakewell, D. Holmes, *Electrophoresis* **2013**, *34*, 987.
[26] D. J. Bakewell, J. Bailey, D. Holmes, *Electrophoresis* **2015**, *36*, 1443.
[27] A. F. Chrimes, A. Kayani, K. Khoshmanesh, P. R. Stoddart, P. Mulvaney, A. Mitchell, K. Kalantar-Zadeh, *Lab. Chip* **2011**, *11*, 921.
[28] T. A. Franke, A. Wixforth, *ChemPhysChem* **2008**, *9*, 2140.
[29] S. Bonhommeau, S. Lecomte, *ChemPhysChem* **2018**, *19*, 8.
[30] K.-T. Liao, C.-F. Chou, *J. Am. Chem. Soc.* **2012**, *134*, 8742.
[31] A. Nakano, A. Ros, *Electrophoresis* **2013**, *34*, 1085.
[32] L. Lesser-Rojas, P. Ebbinghaus, G. Vasan, M.-L. Chu, A. Erbe, C.-F. Chou, *Nano Lett.* **2014**, *14*, 2242.
[33] A. Rohani, B. J. Sanghavi, A. Salahi, K.-T. Liao, C.-F. Chou, N. S. Swami, *Nanoscale* **2017**, *9*, 12124.
[34] L. Velmanickam, M. Fondakowski, I. T. Lima, D. Nawarathna, *Biomicrofluidics* **2017**, *11*, 044115.

[35] N. Swami, C.-F. Chou, V. Ramamurthy, V. Chaurey, *Lab. Chip* **2009**, *9*, 3212.
[36] I.-F. Cheng, S. Senapati, X. Cheng, S. Basuray, H.-C. Chang, H.-C. Chang, *Lab. Chip* **2010**, *10*, 828.
[37] L. Shi, A. Rana, L. Esfandiari, *Sci. Rep.* **2018**, *8*, 6751.
[38] J. H. Moore, W. B. Varhue, Y.-H. Su, S. S. Linton, V. Farmehini, T. E. Fox, G. L. Matters, M. Kester, N. S. Swami, *Anal. Chem.* **2019**, *91*, 10424.
[39] A. Nakano, F. Camacho-Alanis, A. Ros, *Analyst* **2015**, *140*, 860.
[40] A. Castellanos, A. Ramos, *J. Phys. Appl. Phys.* **2003**, *2584*.
[41] J. Sun, Y. Xianyu, X. Jiang, *Chem. Soc. Rev.* **2014**, *43*, 6239.
[42] J. R. G. Navarro, M. H. V. Werts, *Analyst* **2013**, *138*, 583.
[43] A. A. Volkert, V. Subramaniam, M. R. Ivanov, A. M. Goodman, A. J. Haes, *ACS Nano* **2011**, *5*, 4570.
[44] M. H. V. Werts, V. Raimbault, R. Texier-Picard, R. Poizat, O. Français, L. Griscom, J. R. G. Navarro, *Lab. Chip* **2012**, *12*, 808.
[45] M. Loumaigne, C. Midelet, T. Doussineau, P. Dugourd, R. Antoine, M. Stamboul, A. Débarre, M. H. V. Werts, *Nanoscale* **2016**, *8*, 6555.
[46] M. H. V. Werts, V. Raimbault, M. Loumaigne, L. Griscom, O. Français, J. R. G. Navarro, A. Débarre, B. Le Pioufle, *Proc. SPIE* **2013**, *8595*, 85950W.
[47] M. Qi, C. Darviot, S. Patskovsky, M. Meunier, *Analyst* **2019**, *144*, 1303.
[48] J. Yguerabide, E. E. Yguerabide, *Anal. Biochem.* **1998**, *262*, 137.
[49] T. Honegger, PhD thesis, Université de Grenoble, **2011**.
[50] D. J. Bakewell, *J. Phys. Appl. Phys.* **2011**, *44*, 085501.
[51] T. Honegger, D. Peyrade, *Lab. Chip* **2013**, *13*, 1538.
[52] H. Shen, L. J. Tauzin, R. Baiyasi, W. Wang, N. Moringo, B. Shuang, C. F. Landes, *Chem. Rev.* **2017**, *117*, 7331.
[53] P.-Y. Weng, I.-A. Chen, C.-K. Yeh, P.-Y. Chen, J.-Y. Juang, *Biomicrofluidics* **2016**, *10*, 011909.
[54] M. P. Hughes, H. Morgan, M. F. Flynn, *J. Colloid Interface Sci.* **1999**, *220*, 454.
[55] B. C. Gierhart, D. G. Howitt, S. J. Chen, R. L. Smith, S. D. Collins, *Langmuir* **2007**, *23*, 12450.
[56] H. Morgan, N. G. Green, *AC Electrokinetics: Colloids and Nanoparticles*, Research Studies Press, Baldock, **2003**.
[57] W. Ebeling, I. M. Sokolov, *Statistical Thermodynamics and Stochastic Theory of Nonequilibrium Systems*, World Scientific Publishing Company, **2005**.
[58] E. B. Cummings, A. K. Singh, *Anal. Chem.* **2003**, *75*, 4724.
[59] A. Nakano, T.-C. Chao, F. Camacho-Alanis, A. Ros, *Electrophoresis* **2011**.
[60] W. Sutherland, *Lond. Edinb. Dublin Philos. Mag. J. Sci.* **1905**, *9*, 781.
[61] A. Einstein, *Ann. Phys.* **1905**, *322*, 549.
[62] J. Midelet, A. H. El-Sagheer, T. Brown, A. G. Kanaras, M. H. V. Werts, *Part. Part. Syst. Charact.* **2017**, *34*, 1700095.
[63] I. Ermolina, H. Morgan, *J. Colloid Interface Sci.* **2005**, *285*, 419.
[64] J. Lyklema, *Fundamentals of Interface and Colloid Science*, Academic Press, London, **1995**.
[65] S. Basuray, H.-C. Chang, *Phys. Rev. E* **2007**, *75*, 060501.
[66] S. Basuray, H.-H. Wei, H.-C. Chang, *Biomicrofluidics* **2010**, *4*, 022801.
[67] F. G. Halaka, *Proc. Natl. Acad. Sci.* **2003**, *100*, 10164.
[68] G. H. Markx, J. Rousselet, R. Pethig, *J. Liq. Chromatogr. Relat. Technol.* **1997**, *20*, 2857.
[69] Y. Huang, X. B. Wang, F. F. Becker, P. R. Gascoyne, *Biophys. J.* **1997**, *73*, 1118.
[70] O. D. Velev, S. Gupta, *Adv. Mater.* **2009**, *21*, 1897.

[71] A. Soleilhac, M. Girod, P. Dugourd, B. Burdin, J. Parvole, P.-Y. Dugas, F. Bayard, E. Lacôte, E. Bourgeat-Lami, R. Antoine, *Langmuir* **2016**, *32*, 4052.
[72] M. Qi, C. Darviot, S. Patskovsky, M. Meunier, *The Analyst* **2019**, *144*, 1303.
[73] T. E. Oliphant, *Comput. Sci. Eng.* **2007**, *9*, 10.
[74] J. D. Hunter, *Comput. Sci. Eng.* **2007**, *9*, 90.
[75] C. Gohlke, *Tifffile Python*, http://www.lfd.uci.edu/~gohlke.
[76] J. E. Guyer, D. Wheeler, J. A. Warren, *Comput. Sci. Eng.* **2009**, *11*, 6.

S1. Side-illumination of the microfluidic system for dark-field microscopy

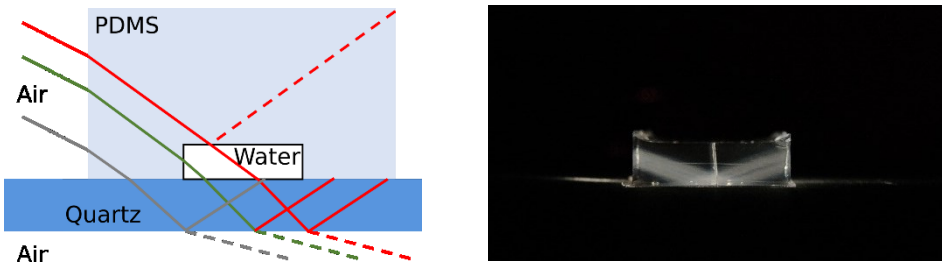

Figure S1. *Left*: The three principal cases of light ray propagation in the microfluidic system for light rays entering the PDMS (n=1.4) slab from the air (n=1) side at a given angle. The angle can be chosen such that there is total internal reflection at the air-quartz (n=1.52)-air interface, but no reflection at the PDMS-water (n=1.33) interface. This holds for angles between 26 and 62 degrees with respect to the normal of the side plane. *Right*: Photograph (side-view) of the light propagation inside the microfluidic system with a weakly focused white-light beam entering the PDMS slab from the left.

S2. Gradual roughening of electrodes when operating at frequencies below 800 kHz

As described in the main text, we observed a more pronounced dielectrophoretic capture of gold nanoparticles on electrodes that had been used for prolonged times, especially using frequencies below 800 kHz for the applied AC electric potential. The more pronounced capture is not due to a local increase at the very tip of the electrode, but due to an extension of the zone of the electrode where the particles are actually captured. For "fresh" electrodes, DEP capture only takes place at the tip, whereas for "aged" electrodes particles are captured all along the electrode contour (Figure S2)

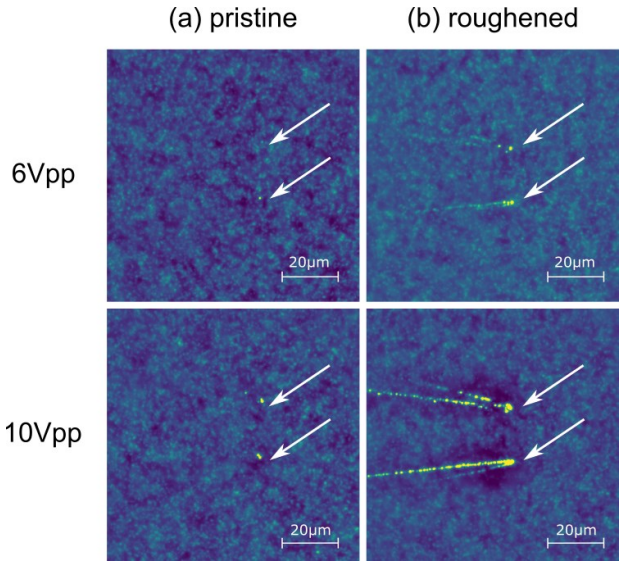

Figure S2. Pictures of the region of interest from a cycle-averaged movie of the DEP of Au100-LA at amplitudes of 6 V_{pp} (top) and 10 V_{pp} (bottom). The brightness and contrast settings (viridis color map) are identical on all image. The white arrows indicate the region of interest. Pair of images on the left: new, pristine electrodes. Pair of images on the right: old electrodes after several cycles of dielectrophoresis at low and high frequency.

We hypothesized that electrochemical roughening of the electrode surface leads to the formation of a multitude of local zones of strong electric field gradient, effectively creating DEP 'hot spots'. This was confirmed by measurements of the electrodes topography by AFM (Figure S3). Dimension 3100 AFM was used, silicon probe tip is mounted to analyse the sample and swept the electrodes by contact.

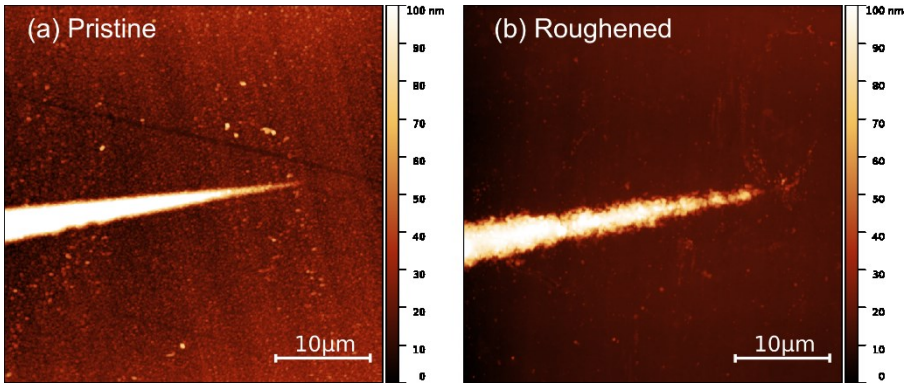

Figure S3. AFM pictures: (a) fresh electrodes after microfabrication; (b) electrodes after many cycles of dielectrophoresis display significant roughness.

Analysis of the AFM profiles (Figure S4), indicates that the electrodes become thinner when aged. This is accompanied by an increase of the roughness.

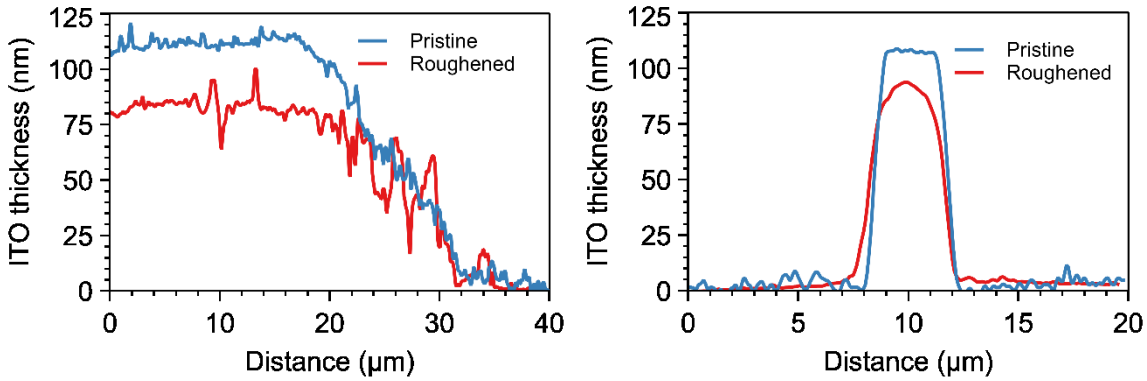

Figure S4. Analysis of AFM pictures. Left: thickness of the ITO along the electrodes. Right: thickness of the ITO the electrodes using a cross-sectional profile (perpendicular to the electrode).

Even though the more pronounced DEP capture on damaged electrodes is visually pleasing in videomicroscopy, because the DEP capture and subsequent release are so clearly observable, we chose to do the DEP measurements using fully intact electrodes where DEP only takes place in a small circular zone centered at the electrode tips. In Table S1 we give the approximate amount of DEP cycles that can be done before the DEP zone starts extending all along the electrodes.

Table S1. Development of electrode roughness as a function of the field amplitude and frequency used. Numbers corresponds to the approximate number of DEP cycles which electrodes could support before damage begins to become apparent.

Frequency (MHz) / Amplitude (Vpp)	**f ≤ 0.8**	**f ≥ 1**
3	100	>> 1000
6	10	1000
10	1	1000

S3. Electrohydrodynamic motion at frequencies below 800 kHz

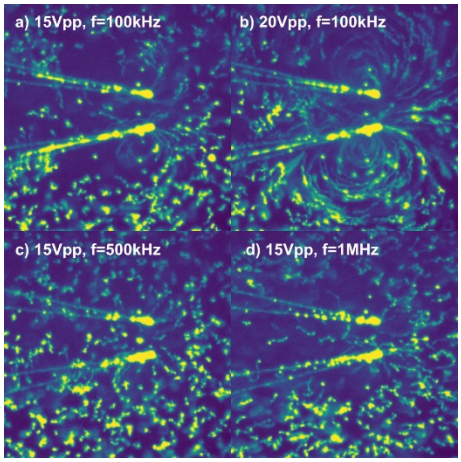

Figure S5. False-colour dark-field videomicroscopy images, averaged over 5 frames, in order to bring out the collective advective motion of the nanoparticles as a function of the parameters of the electric potential applied to the electrode pairs. Electrohydrodynamic flows are discernible for images (a-c). Pure dielectrophoresis is observed for (d).

S4. Device-to-device variations in measured DEP capture ratios

In order to estimate the uncertaintity due to device variations, we measured the same sample (100 nm gold nanospheres in 0.2 mM Na-lipoate, 1 mM NaOH in water) in four separate devices. For each device, at least three independent measurements were carried out over several days. As shown in Figure S6, the measurement of the capture ratio of the same sample in different devices is reproducible to within 20%.

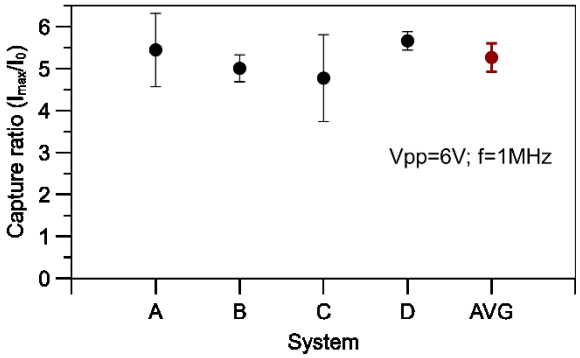

Figure S6. Capture ratio at t = 4 s of particles release as a function of the device at 6 V_{pp} and frequency 1 MHz. Data points indicate individual measurements in different devices. Red data point represents the average of all points. The error bars correspond to 95% confidence interval.

S5. Capture ratios of polystyrene latex spheres as a function of the frequency of the applied electric potential

Figure S7 shows the dependence of the capture ratio for latex particles on the field frequency, at constant amplitude of the applied voltage. From this dependence we can estimate the crossover frequency for each diameter of latex spheres particles. The measurements were done on polystyrene latex particles dispersed in the same medium as the gold nanoparticles (0.2 mM Na-lipoate, 1 mM NaOH in water, conductivity 1 x 10^{-2} S m^{-1})

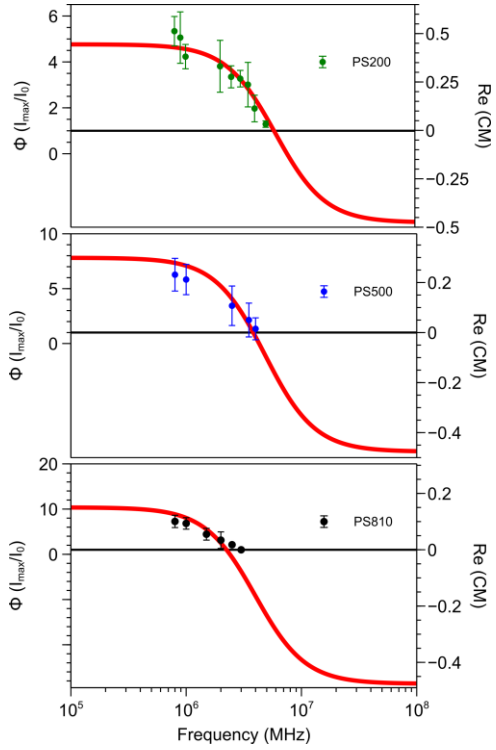

Figure S7. Experimental capture ratios for polystyrene particles (200, 500, 810 nm) as a function of the frequency at 7 V_{pp} to determine the crossover frequency. Red lines correspond to model calculations of the Clausius-Mossotti factor (Equation. S1 and S2), using $\varepsilon_m = 78.5\varepsilon_0$, $\sigma_m = 1 \times 10^{-2}$ S m^{-1}, $\varepsilon_p = 2.55\varepsilon_0$, $\sigma_{p,bulk}$ = 10^{-16} S m^{-1}, and K_s = 1.7 nS (PS200), K_s = 2.8 nS (PS500), K_s = 3.1 nS (PS810).

For low capture ratios, the capture amplitude (= capture ratio minus one) is approximately proportional to the dielectrophoretic force. The behaviour of the capture ratio as a function of electric frequency should therefore follow the trend of the real part of the Clausius-Mossotti

factor (CMF). For this type of polystyrene latex particles, the behaviour of the CMF is well-known, and has been confirmed in many different experiments. [3,4]

The Clausius-Mossotti factor $\tilde{f}_{\mathrm{CM}}$ can be calculated from the complex permittivities $\tilde{\varepsilon}_{m/p}$ according to the equation S1 (subscripts *m* for medium, *p* for particle).[3]

$$\tilde{f}_{\mathrm{CM}} = \frac{\tilde{\varepsilon}_p - \tilde{\varepsilon}_m}{\tilde{\varepsilon}_p + 2\tilde{\varepsilon}_m} \quad with \quad \tilde{\varepsilon}_{p/m} = \varepsilon_{p/m} - i\frac{\sigma_{p/m}}{\omega} \qquad \text{Eq. S1}$$

Where $\sigma_{p/m}$ are the conductivities of the particle and the medium, respectively, and ω is the angular frequency of the applied electric field. In the present case we have $\varepsilon_m = 78.5\varepsilon_0$, $\sigma_m = 1 \times 10^{-2}$ S m^{-1}, and $\varepsilon_p = 2.55\varepsilon_0$.

For the spherical particle, the conductivity σ_p is not only determined by the conductivity of the bulk material but also by its surface conductivity. The overall conductivity of the particles can be calculated from the bulk conductivity of the nanoparticle core material $\sigma_{p,bulk}$ (vanishingly small for polystyrene, ~10^{-16} S m^{-1}), and from the radius a of the particle and its surface conductance K_s. For polystyrene latex particles, the conductivity is dominated by the surface conductivity. We found the overall surface conductivity to vary slightly between different particle diameters, likely due to differing surface densities of ionised groups. All conductivities are within the range typically found for latex particles.[3,5,6]

$$\sigma_p = \sigma_{p,bulk} + \frac{2K_s}{a} \qquad \text{Eq. S2}$$

In the case of sufficiently strong negative DEP, a depletion of particles in the central DEP "capture" zone is expected to occur. We found it difficult to observe this depletion directly, due to low signal to noise ratios for this type of observation. Weak depletion was observed for 200 nm fluorescent polystyrene latex particles (Figure S8), but the low amplitude of the depletion makes systematic measurements of this negative DEP difficult.

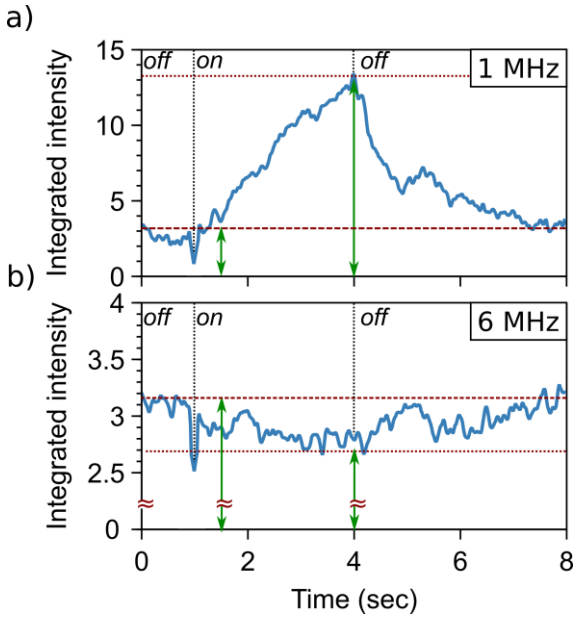

Figure S8. DEP capture-release curves for 200 nm polystyrene particles in aqueous solution at two different frequencies at 7 V_{pp}. The top curve is the curve with capture of particles by positive DEP (1 MHz field frequency). The bottom curve shows weak depletion due to negative DEP (6 MHz field frequency).

The measurement of depletion in the central DEP zone has a poor signal-to-noise ratio. Whereas the amplitude of the concentration of nanoparticles by positive DEP (capture ratio $\phi_{cap} > 1$) can easily become quite large compared to the noise of the measurement in the small central DEP "capture" area, the depletion of nanoparticles in this area by negative DEP leads to capture ratios ϕ_{cap} that are between 1 and 0. Complete depletion would require large negative DEP forces. As a result, such measurements are hampered by noise. For gold nanoparticles, which do not display a cross-over from positive to negative DEP (*e.g.* Figure S9), this is not a limitation, although this difficulty of observing depletion in the central DEP zone does illustrate

that further improvements may be made to the signal-to-noise ratio of the measurement, for example by using more intense illumination sources and more sensitive detection optics, for example by developing a confocal observation of only the DEP-active zone.

S6. Capture ratio of Au100 gold nanoparticles spheres as a function of the applied frequency

To analyze the frequency-dependence of the capture ratio of gold nanoparticles, the frequency was varied from 800 kHz to 6 MHz, and measurements of the capture ratio were made. Figure S9 is a typical result, for 100 nm gold nanospheres. The capture ratio does not depend on frequency. This suggests that the real part of the Clausius-Mossotti is independent of frequency in this range. This is in line with observations using another technique for slightly larger gold nanoparticles,[3] and also with predictions by Gierhart *et al.*[7] The bulk conductivity of the gold nanoparticle core is so high (4.1×10^7 S m^{-1}), completely dominating the dielectric response (via Equations S1 and S2), leading to $\mathrm{Re}\{\tilde{f}_{\mathrm{CM}}\} = 1$ for all frequencies studied.

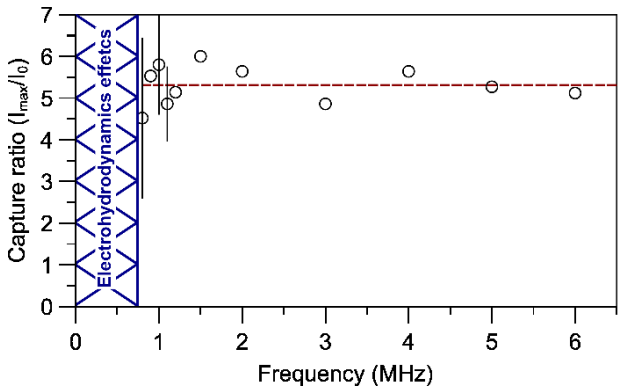

Figure S9. Capture ratio at t = 3 s of Au100-LA as a function of electric field frequency applying an AC electric potential with an amplitude of 6 V_{pp}. The data points indicate the average of individual measurements. The error bars represent the 95% confidence interval. The dotted line is the mean value of all measured capture ratios. Frequencies smaller than 800kHz were not studied due to the appearance of electrohydrodynamic effects that perturb characterization.

S7. Finite-element modelling of the electric field and dielectrophoretic force field experienced by the nanoparticles

Finite-element modelling was used to obtain insight in the topology of the DEP force-field experienced by nanoparticles near the electrodes. Following Equation 2 (Main Text), the effective time-averaged dielectrophoretic force at position $\mathbf{r} = (r_x, r_y, r_z)$ can be calculated from the effective polarizability of the particle $\tilde{\alpha}$, its volume v and the electric field $\mathbf{E}$.

$$\langle \mathbf{F}_{\mathrm{DEP}}(r) \rangle = \frac{1}{4} v \mathrm{Re}[\tilde{\alpha}] \nabla |\mathbf{E}(r)|^2 \qquad \text{Eq. S3}$$

The electric field for our device geometry was calculated from the electrostatic potential obtained by solving the Laplace equation in three dimensions (Comsol Multiphysics software, version 5.2a). The substrate was modelled as silica glass ($\varepsilon_{\mathrm{glass}} = 2.09$). The experimental planar thin-film electrode geometry was reproduced; the electrode tips were rounded with a radius 0.25 μm. The electrodes were approximated as equipotential surfaces by defining the potential at the glass-water interface inside the electrode contours. An applied potential difference of 10 Vpp between the electrodes was used. The medium was water ($\varepsilon_{\mathrm{water}} = 78.5$; $\sigma_m = 1 \times 10^{-2}\ S\ m^{-1}$), enclosed in a chamber of PDMS ($\varepsilon_{\mathrm{PDMS}} = 2.75$) dimensions [$l$, w, h] = [650, 400, 100] μm.

Figure S10 shows maps of the electric field strength, $|\mathbf{E}|$, (top) and the gradient, $\nabla|\mathbf{E}(r)|^2$, (bottom) in a plane at the substrate surface. The latter is proportional to the DEP force. We see that the region of high gradient and high DEP force is concentrated at the tips of the electrodes.

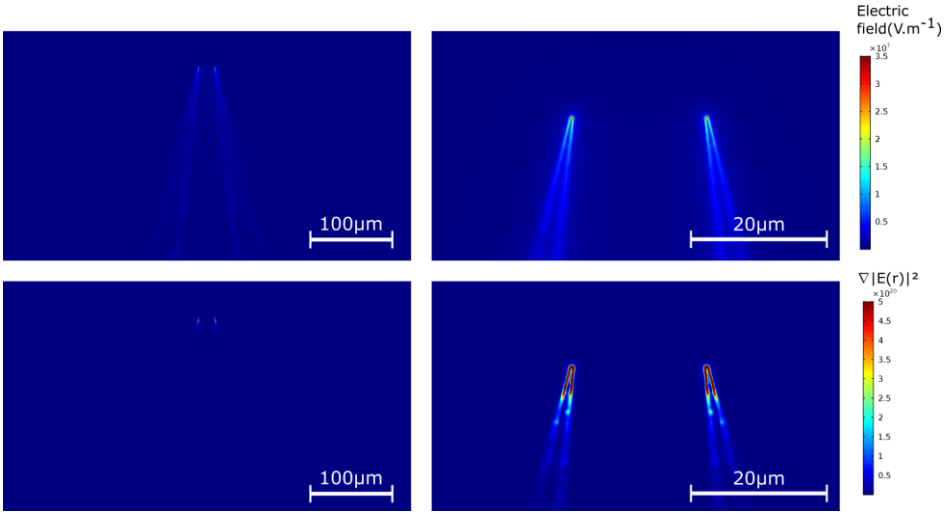

Figure S10. Top: Calculated electrical field strength in the electrode plane of the microchannel. Bottom: Corresponding gradient, $\nabla|\boldsymbol{E}|^2$.

Using the Clausius-Mossotti factor (CMF) and the volume of the gold nanoparticle spheres ($a = 50$ nm), we can calculate the dielectrophoretic force field (which is proportional to $\nabla|\mathbf{E}|^2$and has identical topology). As explained in sections S5 and S6, a CMF of +1 is taken, in line with literature observations.[3,7] For a spherical particle, Equation S3 becomes

$$\langle \mathbf{F}_{\mathrm{DEP}} \rangle = \pi \varepsilon_m r^3 \mathrm{Re}\left[\tilde{f}_{\mathrm{CM}}\right] \nabla|\mathbf{E}|^2 \qquad \text{Eq. S4}$$

The side view of the magnitude of the force is shown in Figure S11. It demonstrates that the force-field is concentrated at the electrode tips. By choosing a lower threshold value of ~ 2 x 10^{-11} N, we can define a "DEP capture zone" that has a radius of 2 µm.

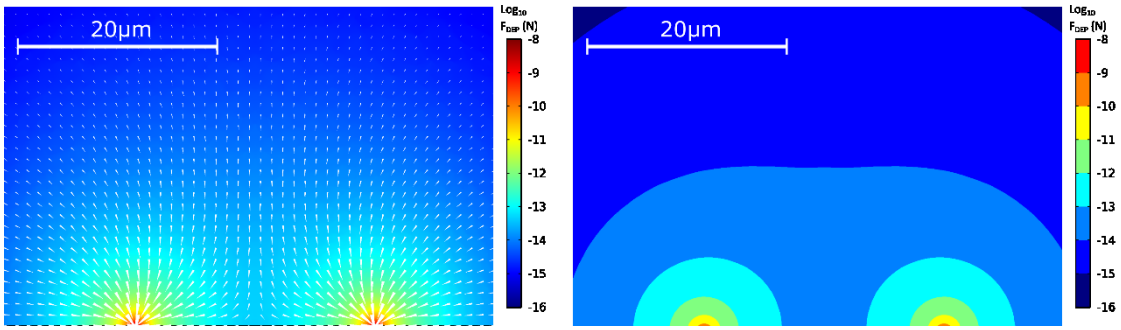

Figure S11. Left: False colour image (side view) of decadic logarithm of the magnitude of the dielectrophoresis force near the electrodes tips. The direction of the force is represented with arrow. Right: False colour image (thresholds applied) with decadic logarithm of DEP forces, demonstrating the radial symmetry of the force-field at the electrode tips.

S10. Optical extinction and scattering spectroscopy of aqueous nanoparticle dispersions

Optical spectroscopy measurements were carried out at ambient temperature on aqueous gold nanoparticle dispersions contained in standard 1 cm quartz or plastic (PMMA) fluorescence cuvettes. UV-visible extinction spectra were measured using an optical fiber-based system (Ocean Optics) incorporating a USB4000-VIS-NIR CCD spectrometer and a LS-1 tungsten halogen light source (6.5W, 3100K). The integrity of the samples was furthermore confirmed using resonant light scattering (RLS) measurements. The RLS measurements were done according to a previously described protocol[1,2] using white light illumination (Avantes, Avalight HAL mini) on samples diluted to an optical density below 0.05. Dilute Ludox was used as the reference (Sigma-Aldrich, Ludox SM30, centrifuged at 9700x *g* for 1 h, supernatant diluted 200x in 10 mM aqueous NaCl). Light scattered by the dispersions was collected at a fixed angle of 90° and analysed using a CCD spectrograph (Ocean Optics QE65000).

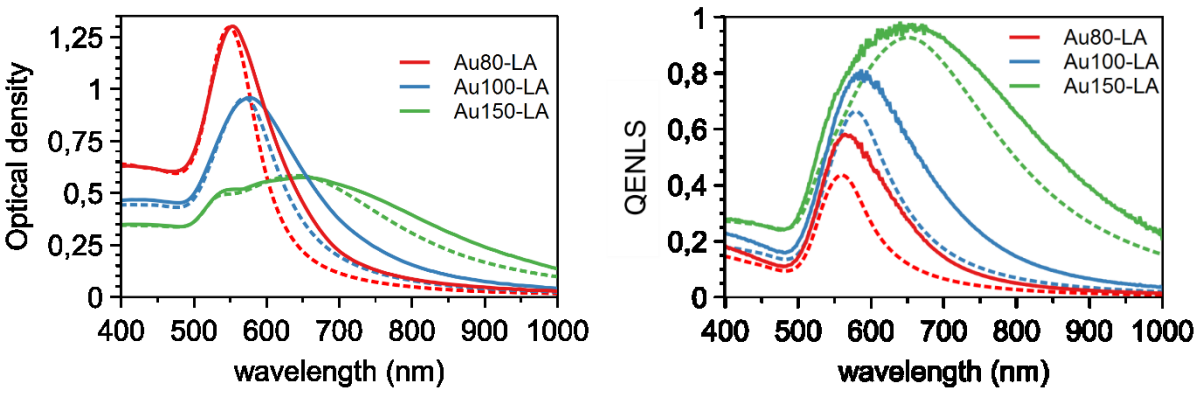

Figure S12. Extinction (left) and light scattering (right) spectra of 150, 100 and 80nm gold nanoparticles coated with lipoate in aqueous solution (1mM NaOH, solid lines). Dotted lines are the results from Mie theory for monodisperse spheres.

References for the supporting information

[1] J. R. G. Navarro, M. H. V. Werts, *Analyst* **2013**, *138*, 583.
[2] M. Loumaigne, C. Midelet, T. Doussineau, P. Dugourd, R. Antoine, M. Stamboul, A. Débarre, M. H. V. Werts, *Nanoscale* **2016**, *8*, 6555.
[3] T. Honegger, K. Berton, E. Picard, D. Peyrade, *Appl. Phys. Lett.* **2011**, *98*, 181906.
[4] N. G. Green, H. Morgan, *J. Phys. Chem. B* **1999**, *103*, 41.
[5] W. M. Arnold, H. P. Schwan, U. Zimmermann, *J. Phys. Chem.* **1987**, *91*, 5093.
[6] M. P. Hughes, H. Morgan, M. F. Flynn, *J. Colloid Interface Sci.* **1999**, *220*, 454.
[7] B. C. Gierhart, D. G. Howitt, S. J. Chen, R. L. Smith, S. D. Collins, *Langmuir* **2007**, *23*, 12450.